Reversible (De) intercalation of Hydrated Zn^{2+} in Mg^{2+}-Stabilized V_2O_5 Nanobelts with High Areal Capacity

Na Wang[1], Congli Sun[2], Xiaobing Liao[2], Yifei Yuan[3], Hongwei Cheng[1,], Qiangchao Sun[1], Bingliang Wang[4], Xuelei Pan[2], Kangning Zhao[1,2], Qian Xu[1], Xionggang Lu[1,*], Jun Lu[3,*]*

N. Wang, H. Cheng, Q. Sun, K. Zhao, Q. Xu, X. Lu

State Key Laboratory of Advanced Special Steel & Shanghai Key Laboratory of Advanced Ferrometallurgy & School of Materials Science and Engineering, Shanghai University, Shanghai 200444, P. R. China

E-mail: hwcheng@shu.edu.cn (H.W. Cheng); luxg@shu.edu.cn (X.G. Lu).

C. Sun, X. Liao, X. Pan, K. Zhao

State Key Laboratory of Advanced Technology for Materials Synthesis and Processing, International School of Materials Science and Engineering, Wuhan University of Technology, Wuhan 430070, China

Y. Yuan, J. Lu

Chemical Sciences and Engineering Division, Argonne National Laboratory, Lemont, Illinois 60439, United States

E-mail: junlu@anl.gov (J. Lu)

B. Wang

Department of Chemistry, Institute of New Energy, iChEM (Collaborative Innovation Center of Chemistry for Energy Materials), Fudan University, Shanghai 200433, P. R. China

Keywords: Zinc-ion battery, $Mg_{0.26}V_2O_5 \cdot 0.73H_2O$, *in-situ* FT-IR spectrum, *in-situ* Raman spectrum, zinc intercalation/deintercalation

Abstract

The rechargeable aqueous zinc ion battery (ZIB) is regarded as one of the most promising candidates for large-scale energy storage applications due to its low-cost and environmental benign properties. However, the development of suitable cathode operating at high rate with high areal capacity and the understanding of reaction mechanisms remain challenging. Herein, we demonstrated the application of $Mg_{0.26}V_2O_5 \cdot 0.73H_2O$ (MVO) nanobelts as a ZIB cathode for hydrated Zn^{2+} intercalation. *In-situ* FT-IR revealed the shift of OH stretching from 3350 cm^{-1} to 3200 cm^{-1}, which corresponds to the hydration shell of Zn^{2+} and conforms to the intercalation of hydrated Zn^{2+} intercalation while *in-situ* Raman suggests the interlayer charge screening effect, which would boost the intercalation of zinc ions in MVO. Density function theory reveals that the insertion of hydrated Zn^{2+}, instead of the naked cations, lowers the Coulombic repulsion at the electrode-electrolyte interface and circumvents the desolvation penalty of hydrated Zn^{2+} during the (de)intercalation process. Additionally, excellent structure stability and large interlayer spacing guarantee the highly reversible (de)intercalation of hydrated zinc ion. In this way, the MVO nanobelts exhibit a high areal capacity of 2.12 mAh cm^{-2} at 0.05 A g^{-1}, outstanding cycling stability of 2500 cycles at 10 A g^{-1} at a high mass loading of 5 mg cm^{-2}. It is believed that the use of hydrated intercalation charge carriers will boost further studies in other multi-valent rechargeable batteries.

Introduction

Due to the increasing demand of energy and the impact of global warming, cutting-edge renewable-energy technology has attracted significant attention [1]. Although lithium ion batteries have achieved great success in the field of portable electronics, their development has been greatly impeded owing to the limited lithium

resources and high cost [2, 3]. In addition, there also arouse safety concerns over combustible organic electrolyte [4]. In this way, the aqueous rechargeable battery with advantages, including low cost, high operation safety, and environmental friendliness, becomes a very promising electrochemical energy storage device [5]. Moreover, the ionic conductivity in the aqueous electrolyte is higher by several orders of magnitude than that in the organic electrolyte [6]. In recent years, much effort has been spent on naturally abundant alkaline ions (Na^+, K^+) as well as bivalent or multivalent ion (Zn^{2+}, Mg^{2+}, and Al^{3+}) battery [7]. Among them, aqueous zinc ion batteries (AZIBs) have attracted increasing interest due to the distinctive merits of zinc metal, especially high theoretical mass and volume capacity (820 mAh g^{-1} and 5885 mAh cm^{-3}, respectively), low redox potential (-0.76 V vs. standard hydrogen electrode), nontoxicity, and excellent chemical stability in aqueous electrolyte [8, 9]. However, AZIBs research is still severely plagued with the limited selection of cathode materials that can demonstrate reversible Zn^{2+}storage after prolonged cycling. Therefore, finding a suitable and stable structure cathode materials that can deliver a stable and favorable capacity for zinc ion storage becomes challenging for AZIBs. Moreover, the gravimetric capacities (mAh g^{-1}) have been focused on most of the recent researches, while other important parameters such as volumetric and areal capacities (mAh cm^{-3} or mAh cm^{-2}) are ignored [10]. In practical, high areal energy is crucial for applications like HEVs and EVs which requires high mass loading of electrode materials. However, recently reported zinc ion battery cathode usually operates at rather low mass loading (0.5-2 mg cm^{-2}), which is far from the standard of commercialization standard, as a low areal capacity below 1 mAh cm^{-2} would be resulted in. Therefore, it remains challenging to develop zinc ion storage electrode materials with high volumetric/areal capacities and able to properly function at high mass loadings (> 5 mg cm^{-2}) [3].

To date, many kinds of researches have been conducted on the cathode materials of aqueous zinc-ion batteries so far [11]. Unfortunately, these electrode materials seriously suffer from poor rate performance, low cycling stability, or limited capacity. Recently, layered and tunnel-type vanadium oxides have been intensively researched as cathode materials for rechargeable aqueous ZIBs [8]. Layered vanadium-based materials have displayed excellent electrochemical performance due to the open-frame crystal structure, large layer spacing, and multiple valence states of vanadium, which allow facile insertion and extraction of Zn^{2+} [12]. However, the unstable structure and poor ion diffusion kinetics lead to unsatisfied cycling performance and rate ability. Tremendous researches were further carried out to optimize the electrochemical performance and several studies suggest that structural water and cationic insertion not only increase the layer spacing but also play important roles in the kinetic to improve the electrochemical performance of the cathode materials [13-16]. Upon the cycle process, the crystallized water in the structure plays a powerful role for the metal ions in electron screening, decreased the interactions of metal ions, and the host frame-works by lowering their effective charge [13, 15, 17]. Meanwhile, pre-intercalation of large metallic ions, such as Ca^{2+}, and Na^{+}, would improve the stability of the aqueous ZIBs. Additionally, the co-insertion of H_2O with Zn^{2+} (The radius of the hydrated zinc ion is 4.3Å [18]) as a hydrated form in the host structures would not only effectively shield divalent charges, but also decrease the desolvation energy associated with the facile hydration of the carrier ion (Zn^{2+}) and consequently lowers the Coulombic repulsion at the electrode-electrolyte interface during the intercalation process [19]. However, there lack analytical tools to directly identify hydrated ions forms that intercalate into the host structure. Additionally, considering the large radius of hydrated zinc ions (4.3Å) [18], the electrode with large layer spacing is expected to design for facile hydrated zinc ion intercalation.

Inspired by these works, we report the $Mg_{0.26}V_2O_5 \cdot 0.73H_2O$ (MVO) nanobelts with a high theoretical areal capacity of 2.3 mAh cm^{-2} at high mass loading over 5 mg cm^{-2}, which corresponds to 1.59 zinc ions intercalation. $Mg_{0.26}V_2O_5 \cdot 0.73H_2O$ delivers high areal capacity (2.3 mAh cm^{-2} at current densities of 50 mA g^{-1}) and long life (capacity retention of 98% over 2500 cycles at 10 A g^{-1}), which outperforms previously reported vanadium-based zinc ion battery cathode (Tab. S1). More importantly, the intercalation of hydrated Zn^{2+} ions is revealed by *in-situ* Raman and *in-situ* FT-IR. The co-intercalation of zinc ions and water molecules into the host plays a vital role in enhancing the electrochemical performance by facilitating Zn ion diffusion *via* interlayer shielding electrostatic interactions and avoiding the desolvation penalty. Our study suggests hydrated ion intercalation is the key to enhancing the structural dynamics of electrode materials in aqueous electrolytes and ultimately developing high performance aqueous battery systems in the near future.

Results and Discussion

Initially, the X-ray diffraction (XRD) pattern of the as-prepared sample and the Rietveld refinement result are shown in Fig. 1a. Refined parameters are calculated to be a = 10.59 Å, b = 8.03 Å, c = 13.39 Å, α = 91.39°, β = 90.77°, γ = 88.86° (Tab. S2). In the XRD pattern, there are only six peaks observed all of which can be assigned to (00*l*) reflections, suggesting the high crystallinity and preferential growth in (00*l*) plane. Moreover, no other peaks are observed, indicating the high phase purity. The (001) peak at 2θ = 6.76°, corresponds to a large layer spacing of 12.3 Å, which is believed to be beneficial to the extraction and insertion of Zn^{2+} during charge/discharge process. The XRD pattern of VO is shown in Fig. S1 (JCPDS No. 075-0457). The inserted Mg^{2+} and crystalized water in the bilayered vanadium structure act as pillars to stabilized the

layered structure (Fig. 1a inset and Fig. 1b). The content of crystallized water is determined via the thermogravimetric (TGA) curve (Fig. 1c), the weight loss before 100 ℃ is attributable to the absorption water, and the weight loss from 100 ℃ to 400 ℃ corresponds to the crystallized (structural) water in MVO materials, which shows a weight reduction of 1.0%, 6.5%, respectively. Inductively coupled plasma optical emission spectroscopy (ICP-OES) further reveals that the molecular formula of the as-prepared material is $Mg_{0.26}V_2O_5 \cdot 0.73H_2O$ (Tab. S3). The morphology of the two samples is revealed by scanning electron microscopy (SEM). MVO is composed of homogeneous nanobelts with a diameter of 200~300 nm and a length of 5~10 μm, while VO consists of nanowires (Fig. S2, S3). Both MVO and VO show a smooth surface. STEM and EDS element mappings are implemented to further study the morphology and crystal structures of the MVO sample. The STEM image of MVO displays a belt-like morphology with a diameter of ~300 nm (Fig. 1d). The HRTEM image shows a lattice fringe clearly with a spacing of 0.26 nm, corresponding to the (601) lattice plane of MVO (Fig. 1e). From the selected area electron diffraction (SAED) image, the single-crystalline of MVO with high crystallinity was displayed (Fig. 1f). The selected area electron diffraction ring patterns in the lower left corner of Figure 1e are well assigned to the (001), (020) planes of layered structure of MVO materials. The EDS element mappings reveal the uniform distribution of Mg, V, and O elements, confirming the existence of Mg^{2+} in MVO (Fig. 1g).

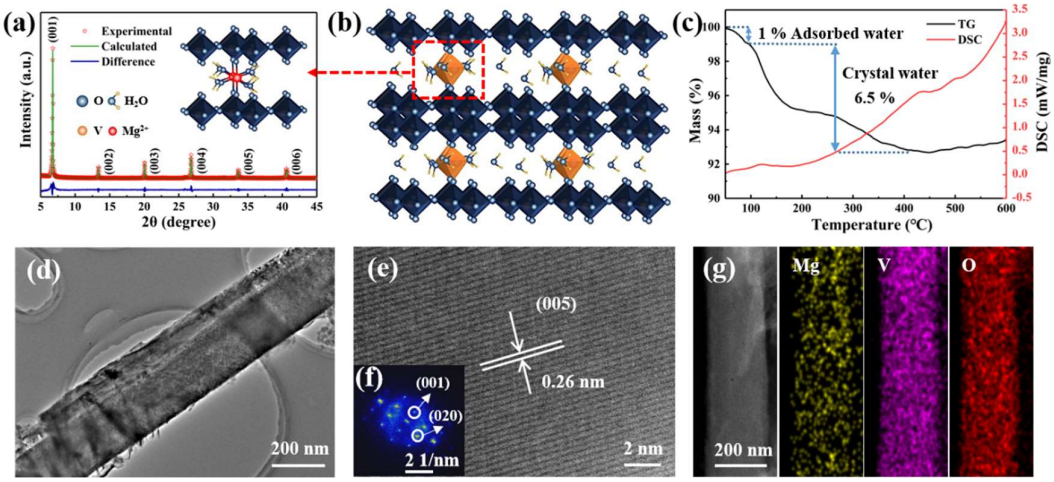

Fig. 1. Characterization of MVO nanobelts: (a) Rietveld refinement result of the MVO XRD pattern and (b) the corresponding $Mg_{0.26}V_2O_5{\cdot}0.73H_2O$ crystal structure; (c) TGA-DSC curves; (d) TEM image; (e) HRTEM image; (f) SAED pattern; and (g) EDS element mappings of MVO nanobelts.

The zinc storage performance of MVO is evaluated in the potential window of 0.1-1.8 V. Initially, the CV measurement was implemented at a scan rate of 1 mV s^{-1} (Fig. 2a). Three pairs of redox peaks are located at 1.44/1.35, 1.24/1.08, and 0.67/0.56 V, respectively, indicating a multistep reaction process concerning (de)intercalation of Zn^{2+}. The largely overlapping of the initial three CV cycles illustrates the excellent reversibility of Zn^{2+} interaction/extraction, which is further proved by the nearly reversible initial three charge/discharge cycles at 0.05 A g^{-1} (Fig. 2b). Nevertheless, the initial three CV cycles of VO is shown in Fig. S4 exhibits fewer redox peak pairs (1.28/0.82, 1.02/0.38 V), which suggest fewer insertion sites of Zn^{2+}. Fig. S4 indicates the poor reversibility and structural stability of the VO electrode. As we focus on the high mass loading (above 5 mg cm^{-2}) and high areal capacity (above 2 mAh cm^{-2}), the capacity is plotted as areal capacity in our electrochemical performance. The corresponding gravity capacity is plotted in Fig. S7. As shown in Fig. 2b, a high areal capacity of 2.12 mAh cm^{-2} is achieved at the low current density of 50 mA g^{-1}.

While the first three cycles of charge-discharge curves of VO presents poor cycle performance (Fig. S5). It is worth noting that MVO exhibits the highest areal capacity among those recently reported vanadium-based cathodes for ZIB in Fig. S6 and Tab. S1. The rate performance of MVO and VO are shown in Fig. 2d. The MVO exhibits high capacities of 2.1, 1.7, 1.3, 1.15, 0.63, and 0.38 mAh cm^{-2} at the current densities of 0.05, 0.1, 1, 2, 5, and 10 A g^{-1}, respectively. After the current returning to 0.1 A g^{-1}, no obvious capacity decay is observed, while the VO electrode delivers much lower specific capacity at each current density and suffers a rapid capacity decay (from 1.5 to 1.25 mAh cm^{-2}) when the current density is returned to 0.1 A g^{-1}. Fig. 2e displays the charge-discharge curves of MVO under various current densities. Apart from the good rate capability, MVO also displays excellent long-term cyclic stability. In Fig. 2c, the initial discharge capacity of MVO is 1.77 mAh cm^{-2} and after 100 cycles the capacity retention is over 93% with a Coulombic efficiency close to 100%. However, although the VO electrode displays a high initial capacity of 1.79 mAh cm^{-2}, it suffers serious capacity fading with a poor capacity retention of only 38% after only 55 cycles and unsatisfactory Coulombic efficiency (94%) (The gravity capacity of MVO and VO are shown in Fig. S7). The same phenomenon is observed at higher rates of 1 and 5 A g^{-1} in Fig. 2f and 2g, respectively. The increase in capacity of the first 20 cycles may be attributed to the activation of the electrode at high current densities [20]. The activation process is benefited to associated with the electrode wetting in the electrolyte and the enhancement of ion-transport during cycling. This phenomenon is believed to be linked to the incomplete infiltration of the electrolyte with the electrode. The MVO electrode presents a maximum areal capacity of 0.75 mAh cm^{-2} with capacity retention > 98% over 2000 cycles. Even at a large current density of 10 A g^{-1}, a capacity of about 0.5 mAh cm^{-2} is still retained while there is a slight increase after 2500 cycles, indicating

the outstanding cycling stability (Fig. S8). The SEM images of MVO after 200 cycles at 0.1 A g^{-1} (Fig. S9a) and 2500 cycles at 10 A g^{-1} (Fig. S9b) exhibit that the nanobelts morphology is well maintained, indicating the excellent stability of the structure.

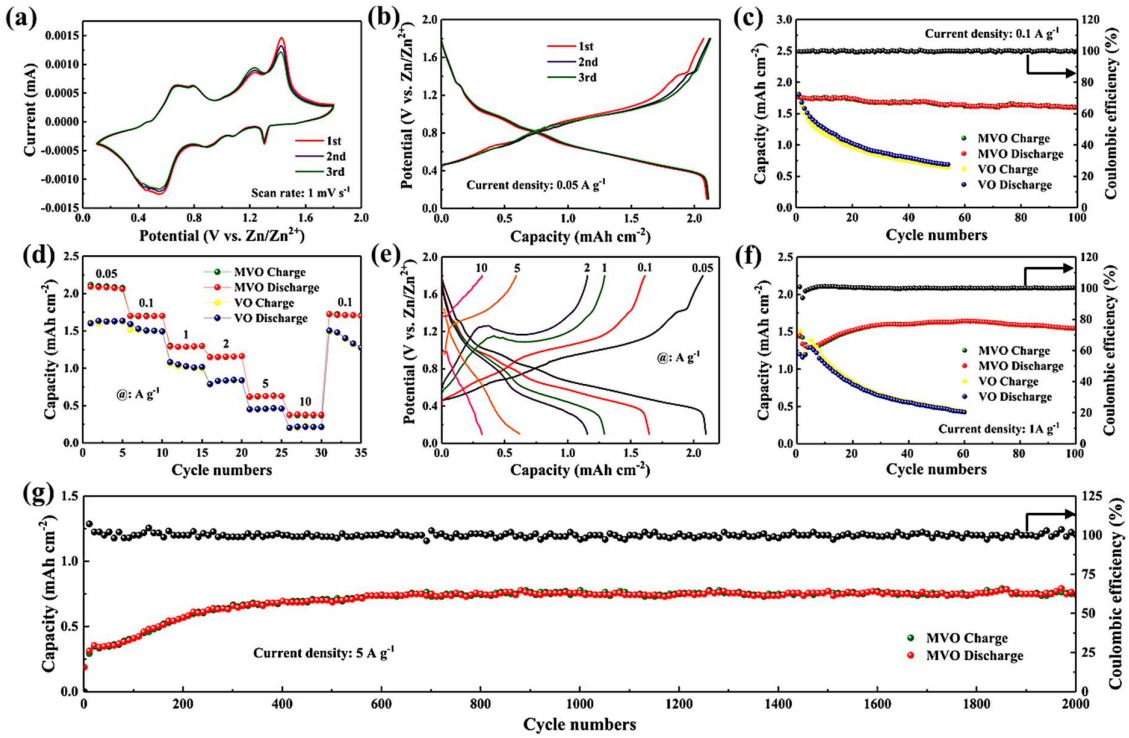

Fig. 2. Electrochemical performance of the MVO and VO electrodes: (a) CV curves of MVO electrode; (b) charge/discharge curves of MVO at 0.05 A g^{-1}; (d) rate performance of MVO; (e) charge/discharge of MVO at different rates; (c), (f) and (g) cycling performance at 0.1, 1, and 5 A g^{-1}, respectively.

Multiple *in-situ* and *ex-situ* characterizations were carried out to gain insight into the Zn^{2+} storage mechanism of the MVO electrode. The *ex-situ* XRD patterns at different discharged-charged states in the first cycle at 0.1 A g^{-1} is shown in Fig. 3a. First, during the discharge process to 0.1 V, a small contraction of interlayer spacing is observed (Fig. 3a). This is because the inserted hydrated Zn^{2+} will screen the interlayer

electrostatic repulsion as the hydrated Zn^{2+} content increases. Furthermore, the hydrated Zn^{2+} would result in the formation of hydrogen bonding, which leads to the shrinkage of the layer. Moreover, a new phase formation is captured at a voltage below 0.5 V, with a layer spacing of 9.8 Å. This phenomenon is similar to the previous report ($Mg_xV_2O_5 \cdot nH_2O$) in which two phases co-exist at a voltage below 0.8 V [15, 21]. The new phase formation is believed to be related to the overwhelmed hydrated zinc ions intercalation, which breaks the hydrogen bonding between layer and hydrated zinc ions and leads to the expansion of the layered structure to 14.2 Å. On the contrast, during the charging process, these peaks nearly recover to their initial position, demonstrating that the structural change of MVO upon the charge/discharge process is highly reversible, which ensures good cycling stability. The XPS results show intercalation/deintercalation of Zn^{2+} and changes in the valence state of V during the cycles. As shown in Fig. 3b, there is no signal of Zn^{2+} being detected in the original electrode. Nevertheless, the Zn 2p peak in the fully discharged state is sharp and strong, indicating the successful insertion of Zn^{2+}. Instead, a weak peak of Zn 2p can be observed in the fully charged state, which indicates the extraction of Zn^{2+}. In the V 2p XPS region, the reversible electrochemical reduction can be discovered obviously due to the $Zn^{2+}/2e^-$ intercalation (Fig. 3c). In the fully discharged state, the V^{4+} signal intensifies strongly upon, and even appears a V^{3+} component, according to the electrochemical reaction principle based on the insertion of Zn^{2+}. Yet, the original V 2p spectrum is regenerated in the fully charged state nearly. These interactions lead to a moderate bonding rearrangement and lightly structural stress rendering excellent rate performance and cyclability. The *ex-situ* STEM is implemented to further explore the (de)intercalation behaviors of Zn^{2+}. The STEM images (Fig. 3d, Fig. 3g) display clear and uniform nanobelts, indicating a stable morphology during cycling. During the discharge, there observed two phases in the NW body. The

major part shows a decreased lattice fringes of 0.248 nm, which is consensus with the *ex-situ* XRD pattern in which a phase sepearation recation is captured at discharged state with two layered strucature co-existance in the electrode. The minor part on the surface with a lattice fringe of 0.267 nm (Fig. 3f). The minor phase formation shows enlarged lattice spacing, which is believed to be related to the overwhelmed hydrated zinc ions intercalation, which breaks the hydrogen bonding between layer and hydrated zinc ions. Compared to the initial state (0.26 nm), the layer spacing is fully discharged of the first cycle decreased to 0.248 nm (Fig. 3f), which certifies the insertion of Zn^{2+} and coincide well with EDS element mappings shown in Fig. 3e. Meanwhile, the layer spacing restored to 0.254 nm in fully charged after three cycles (Fig. 3i), consensus to the *ex-situ* XRD results. The EDS element mapping result for the fully-charged state after three cycles (Fig. 3h) presents that there is no obvious Mg loss in the nanobelt body, suggesting that the Mg ions are stable in the host and act as a pillar for zinc ions intercalation. The EDS quantification of elements is shown in Fig. S10 confirming the stable Mg ions and intercalation of Zn ions into the nanowires. This is also confirmed by Energy dispersive X-ray (EDX) spectra of the Zn anode after 200 cycles at the current density of 1 A g^{-1} (Fig. S11). No Mg trace is detected on the Zn anode surface confirming the stable Mg ions in the layered structure.

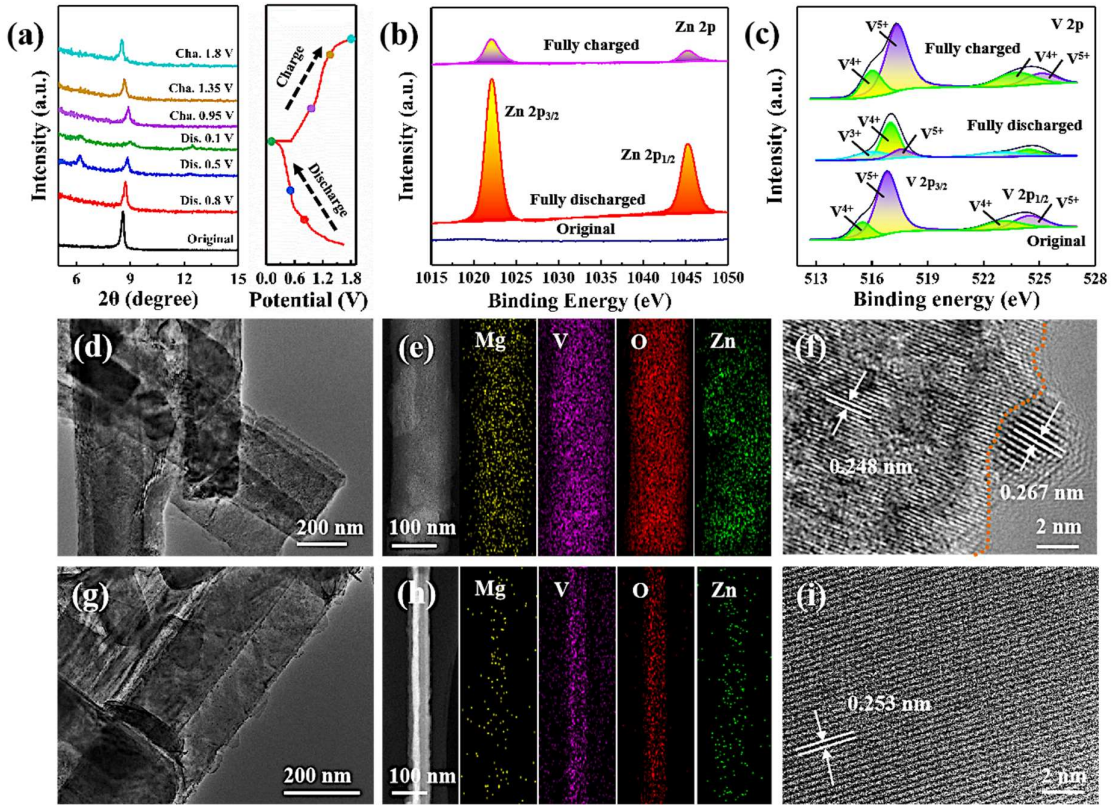

Fig. 3. The *ex-situ* XRD, XPS and STEM study of MVO nanobelts: (a) *ex-situ* XRD patterns at different charge/discharge states and corresponding GCD curves at 0.1 A g^{-1}; (b), (c) XPS spectra of Zn 2p (b) and V 2p (c) regions in different states; (d)-(f) STEM images, EDS element mapping images and HRTEM image in the fully discharged state of the first cycle; (g)-(i) STEM image, EDS element mapping images, and HRTEM image in the fully charged state after three cycles.

In-situ Raman and *in-situ* FT-IR analysis provide further proof. The FT-IR spectrum of the original state electrode exhibits clearly the mode located at 819 cm^{-1}, which corresponds to the asymmetric stretching modes of V-O-V of bridged oxygen. Fig. 4a exhibits the dynamic change of the FT-IR spectrum in the first charging (from 0.1 V to 1.8 V) and discharging (from 1.1 V to 0.1 V) cycle. In the process of discharge, the mode located at 819 cm^{-1} blue shift occurs, The blue shift of the peak at 819 cm^{-1} suggests that during the discharge,

the asymmetric stretching of V-O-V gradually increases, confirming the zinc ion intercalation into the layer of MVO. In the process of charge, the peak is turned back to its original state, suggesting the excellent reversibility and stability of the layered structure. On the other hand, an interesting phenomenon is observed at high frequency. During charging, the peak at 3350 cm^{-1} which corresponds to the OH stretching of crystalized water gradually decreases while the peak at ~3200 cm^{-1}, which corresponds to the OH stretching of the hydration shell of Zn^{2+} intensifies [22], while during discharging, *vise visa*, confirming the (de)intercalation hydrated Zn^{2+} during (dis)charging (Fig. 4b). The *in-situ* Raman spectra of the first three discharge/charge processes are shown in Fig. 4c. Four distinct peaks located at 778, 573, 344, and 314 cm^{-1} are observed, which correspond to Ag, (Ag + Bg), Ag, and Bg of asymmetric V-O-V bridges [23]. All the peaks show similar trends. The intensities of all peaks gradually decay in the fully discharged state and reach the maximum in the fully charged state. The largely decreased intensity is believed to be associated with the charge screening effect induced by the hydrated Zn^{2+} in aqueous electrolyte. Moreover, by magnifying the weak peaks during the discharged state, the peak positions undergo redshift, suggesting an increase in the restoring force as a consequence of tensile stress in MVO and confirming the intercalation of hydrated Zn^{2+} [24]. This is also confirmed by the *ex-situ* FT-IR spectrum in Fig. 4d. All the results suggest the reversible insertion of hydrated Zn^{2+} into MVO. The schematic illustration of (de)intercalation mechanism of solved Zn^{2+} is shown in Fig. 4e. The hydrated zinc ion intercalation into the MVO host is confirmed by *in-situ* Raman and *in-situ* FT-IR. We then performed density functional theory (DFT) calculations to evaluate the intercalation behavior of Zn^{2+} in MVO. We have systematically investigated the correlation between hydration level and the intercalation energy. With large interlayer spacing, the MVO is able to incorporate Zn^{2+} cations

with 6 water molecules as a solvation shell, suggesting that there will be no need for desolvation of Zn^{2+} during intercalation process, which is consensus to the *in-situ* and *ex-situ* FT-IR results. In this way, the intercalation energy can be lowered. On the contrast, the naked zinc ion, which is free from the desolvation energy, requires more intercalation energy compared with hydrated zinc ion, which is not conductive to the (de)intercalation process (Fig. 4f). By taking the advantages of hydrated zinc ion intercalation, MVO realizes fast hydrated zinc ion storage capability through avoiding the desolation penalty. The co-insertion of H_2O with carrier ions in the host structures can not only effectively shield divalent charges, but also decrease the desolvation energy associated with the facile hydration of the carrier ion (Zn^{2+}) and consequently lowers substantially the Coulombic repulsion at the electrode-electrolyte interface during the intercalation process. Additionally, the stable Mg ions in the layered structure act as "pillar" for the excellent structure stability and large interlayer spacing, which contributed the stable cycling performance. In this way, the MVO realizes the high areal capacity, outstanding rate capability, and excellent cyclability.

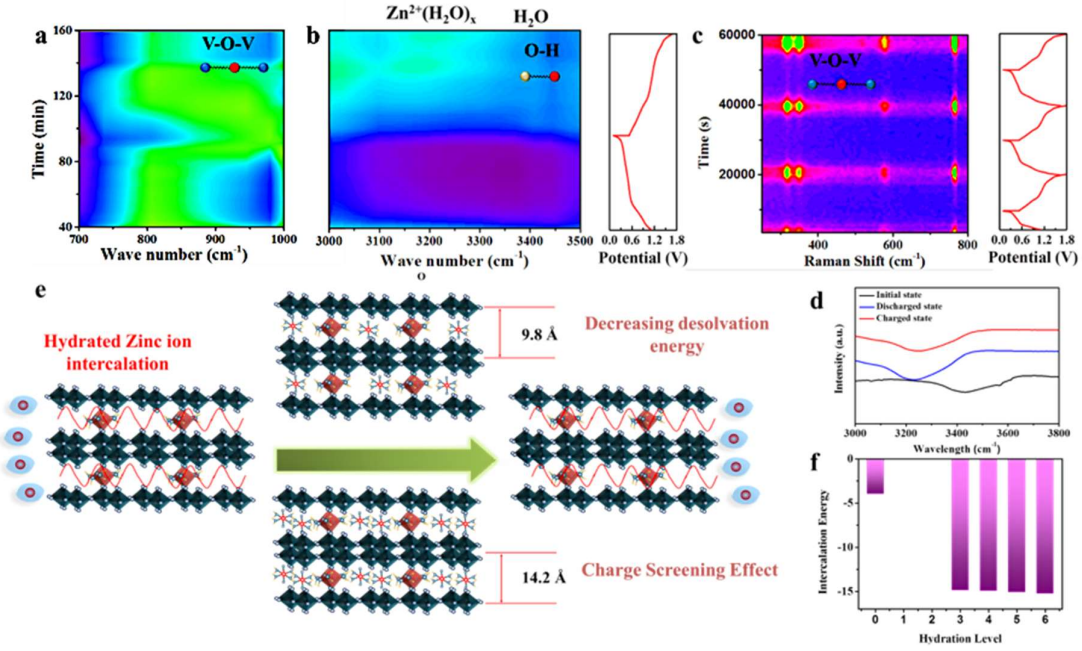

Fig. 4. (a), (b) Electrochemical *in-situ* FT-IR characterization of MVO electrode; (c) electrochemical *in-situ* Raman characterization of MVO electrode; (d) *Ex-situ* FT-IR spectrum of MVO electrode at different state; (e) Schematic illustrations of (de)intercalation mechanism of solved Zn^{2+}; (f) Theoretically calculated effective energy against the hydration level of Zn^{2+}.

Conclusions

In summary, through various *in-situ* and *ex-situ* analytical techniques and electrochemical evaluations, the hydrated Zn^{2+} intercalation into the $Mg_{0.26}V_2O_5{\cdot}0.73H_2O$ (MVO) nanobelts is confirmed. The role of hydrated zinc ion intercalation was confirmed by in-situ FT-IR and DFT calculation reveals MVO takes the advantages low desolvation energy by means of insertion of the hydrated zinc ion. The charge screening effect during the zinc ion intercalation is also verfied by *in-situ* Raman. Utilizing the insertion of the hydrated zinc ions, MVO takes the advantages of charge screening effect and low desolvation energy. Meanwhile, the stable Mg ions in the layer structure facilitate the excellent structure flexibility and large interlayer spacing, enabling the highly reversible intercalation and deintercalation of hydrated zinc ion. In this way, the MVO nanobelts exhibit the high areal capacity of 2.12 mAh cm^{-2} at 0.05 A g^{-1}, outstanding cycling stability and rate capability of 2500 cycles at 10 A g^{-1} at a high mass loading of 5 mg cm^{-2}. It is believed that our findings on the utilizing of hydrated intercalation charge carriers into large layer spacing cathodes to avoid the desovation penalty will boost further researches in other aqueous batteries field.

Supporting Information

Supporting Information is available from the Wiley Online Library or the author.

Acknowledgements

N.W., C. S., and X.L. contributed equally. We gratefully acknowledge financial support from the National Natural Science Foundation of China (Nos. 51874196, 21905169, 51674164), sponsored by the Shanghai Pujiang Program (2019PJD015), the Iron and Steel Joint Research Fund of National Natural Science Foundation and China Baowu Steel Group Corp. Ltd (U1860203), the Science and Technology Commission of Shanghai Municipality (No. 19DZ2270200) and CAS Interdisciplinary Innovation Team. Work at Argonne National Laboratory was supported by the U. S. Department of Energy (DOE), Office of Energy Efficiency and Renewable Energy, Vehicle Technologies Office. Argonne National Laboratory is operated for DOE Office of Science by UChicago Argonne, LLC, under contract number DE-AC02-06CH11357.

Received: ((will be filled in by the editorial staff))
Revised: ((will be filled in by the editorial staff))
Published online: ((will be filled in by the editorial staff))

References

[1] a) R. Van Noorden, Nature 2014, 26; b) C. Zhu, R. Usiskin, Y. Yu, J. Maier, Science 2017, 358, 1400; c) K. Zhao, M. Wen, Y. Dong, L. Zhang, M. Yan, W. Xu, C. Niu, L. Zhou, Q. Wei, W. Ren, Advanced Energy Materials 2017, 7, 1601582.

[2] a) Y. Zhao, L. V. Goncharova, A. Lushington, Q. Sun, H. Yadegari, B. Wang, W. Xiao, R. Li, X. Sun, Advanced Materials 2017, 29, 1606663; b) W. Luo, C.-F. Lin, O. Zhao, M. Noked, Y. Zhang, G. W. Rubloff, L. Hu, Advanced Energy Materials 2017, 7, 1601526; c) C. Sun, X. Liao, F. Xia, Y. Zhao, L. Zhang, S. Mu, S. Shi, Y. Li, H. Peng, G. V. Tendeloo, ACS nano 2020, doi: 10.1021/acsnano.0c02237.

[3] L. Zhang, K. Zhao, C. Sun, R. Yu, Z. Zhuang, J. Li, W. Xu, C. Wang, W. Xu, L. Mai, Energy Storage Materials 2020, 25, 376.

[4] C. Sun, X. Liao, F. Xia, Y. Zhao, L. Zhang, S. Mu, S. Shi, Y. Li, H. Peng, G. Van Tendeloo, ACS nano 2020, 14, 6181.

[5] a) J. O. G. Posada, A. J. R. Rennie, S. P. Villar, V. L. Martins, J. Marinaccio, A. Barnes, C. F. Glover, D. A. Worsley, P. J. Hall, Renewable and Sustainable Energy Reviews 2017, 68, 1174; b) J. Liu, C. Xu, Z. Chen, S. Ni, Z. X. Shen, Green Energy & Environment 2017; c) C. Yang, X. Ji, X. Fan, T. Gao, L. Suo, F. Wang, W. Sun, J. Chen, L. Chen, F. Han, L. Miao, K. Xu, K. Gerasopoulos, C. Wang, Advanced Materials 2017, 1701972.

[6] a) J. F. Parker, C. N. Chervin, I. R. Pala, M. Machler, M. F. Burz, J. W. Long, D. R. Rolison, Science 2017, 356, 415; b) Z. Yu, B. Wang, X. Liao, K. Zhao, Z. Yang, F. Xia, C. Sun, Z. Wang, C. Fan, J. Zhang, Advanced Energy Materials 2020, 2000907.

[7] a) X. Shan, D. S. Charles, Y. Lei, R. Qiao, G. Wang, W. Yang, M. Feygenson, D. Su, X. Teng, Nature Communications 2016, 7, 13370; b) P. Lu, Y. Sun, H. Xiang, X. Liang, Y. Yu, Advanced Energy Materials 2018, 8, 1702434 ; c) M. Liu, Z. Rong, R. Malik, P. Canepa, A. Jain, G. Ceder, K. A. Persson, Energy Environ. Sci. 2015, 8, 964; d) M. Liu, A. Jain, Z. Rong, X. Qu, P. Canepa, R. Malik, G. Ceder, K. A. Persson, Energy & Environmental Science 2016, 9, 3201; e) P. Canepa, G. Sai Gautam, D. C. Hannah, R. Malik, M. Liu, K. G. Gallagher, K. A. Persson, G. Ceder, Chemical Reviews 2017, 117, 4287; f) K. Zhao, C. Wang, Y. Yu, M. Yan, Q. Wei, P. He, Y. Dong, Z. Zhang, X. Wang, L. Mai, Advanced Materials Interfaces 2018, 5.

[8] a) H. Pan, Y. Shao, P. Yan, Y. Cheng, K. S. Han, Z. Nie, C. Wang, J. Yang, X. Li, P. Bhattacharya, K. T. Mueller, J. Liu, Nature Energy 2016, 1, 16039; b) D. Kundu, B. D. Adams, V. Duffort, S. H. Vajargah, L. F. Nazar, Nature Energy 2016, 1, 16119.

[9] a) S. Lian, C. Sun, W. Xu, W. Huo, Y. Luo, K. Zhao, G. Yao, W. Xu, Y. Zhang, Z. Li, K. Yu, H. Zhao, H. Cheng, J. Zhang, L. Mai, Nano energy 2019, 62, 79; b) W. Xu, K. Zhao, W. Huo, Y. Wang, G. Yao, X. Gu, H. Cheng, L. Mai, C. Hu, X. Wang, Nano energy 2019, 62, 275; c) T. N. T. Tran, D. Aasen, D.

Zhalmuratova, M. Labbe, H. J. Chung, D. Ivey, Batteries & Supercaps 2020; d) L. Kang, M. Cui, Z. Zhang, F. Jiang, Batteries & Supercaps; A. Dhiman, D. G. Ivey, Batteries & Supercaps 2020.

[10] M. Nawwar, R. Poon, R. Chen, R. P. Sahu, I. K. Puri, I. Zhitomirsky, Carbon Energy 2019, 1, 124.

[11] a) V. Renman, D. O. Ojwang, M. Valvo, C. P. Gómez, T. Gustafsson, G. Svensson, Journal of Power Sources 2017, 369, 146; b) R. Trócoli, F. La Mantia, ChemSusChem 2015, 8, 481; c) L. Zhang, L. Chen, X. Zhou, Z. Liu, Advanced Energy Materials 2015, 5, 1400930.

[12] a) H. Tang, Z. Peng, L. Wu, F. Xiong, C. Pei, Q. An, L. Mai, Electrochemical Energy Reviews 2018, 1, 169; b) M. H. Alfaruqi, V. Mathew, J. Song, S. Kim, S. Islam, D. T. Pham, J. Jo, S. Kim, J. P. Baboo, Z. Xiu, K.-S. Lee, Y.-K. Sun, J. Kim, Chemistry of Materials 2017, 29, 1684; c) D. Chao, C. Zhu, M. Song, P. Liang, X. Zhang, N. H. Tiep, H. Zhao, J. Wang, R. Wang, H. Zhang, H. J. Fan, Adv. Mater. 2018, 30, 1803181.

[13] X. Ji, J. Chen, F. Wang, W. Sun, Y. Ruan, L. Miao, J. Jiang, C. Wang, Nano letters 2018, 18, 6441.

[14] Y. Liu, C. Li, J. Xu, M. Ou, C. Fang, S. Sun, Y. Qiu, J. Peng, G. Lu, Q. Li, J. Han, Y. Huang, Nano Energy 2020, 67, 104211.

[15] M. Yan, P. He, Y. Chen, S. Wang, Q. Wei, K. Zhao, X. Xu, Q. An, Y. Shuang, Y. Shao, Advanced Materials 2018, 30, 1703725.

[16] Q. Zhao, L. Liu, J. Yin, J. Zheng, D. Zhang, J. Chen, L. Archer, Angewandte Chemie International Edition 2019.

[17] a) H. Liang, Z. Cao, F. Ming, W. Zhang, D. H. Anjum, Y. Cui, L. Cavallo, H. N. Alshareef, Nano letters 2019, 19, 3199; b) F. Wang, W. Sun, Z. Shadike, E. Hu, X. Ji, T. Gao, X. Q. Yang, K. Xu, C. Wang, Angewandte Chemie International Edition 2018, 57, 11978.

[18] E. Nightingale Jr, The Journal of Physical Chemistry 1959, 63, 1381.

[19] a) J. Shin, D. S. Choi, H. J. Lee, Y. Jung, J. W. Choi, Advanced Energy Materials 2019, 9, 1900083; b) L. E. Blanc, D. Kundu, L. F. Nazar, Joule 2020; c) K. W. Nam, H. Kim, Y. Beldjoudi, T.-w. Kwon, D. J. Kim, J. F. Stoddart, Journal of the American Chemical Society 2020; d) R. Yuksel, O. Buyukcakir, W. K. Seong, R. S. Ruoff, Advanced Energy Materials 2020, 10, 1904215.

[20] Q. Pang, C. Sun, Y. Yu, K. Zhao, Z. Zhang, P. M. Voyles, G. Chen, Y. Wei, X. Wang, Advanced Energy Materials 2018, 8, 1800144.

[21] F. Ming, H. Liang, Y. Lei, S. Kandambeth, M. Eddaoudi, H. N. Alshareef, ACS Energy Letters 2018, 3, 2602.

[22] a) X. Yuan, C. Zhang, Computational and Theoretical Chemistry 2020, 1171, 112666; b) A. Patra, S. Roy, S. Saha, D. K. Palit, J. A. Mondal, The Journal of Physical Chemistry C 2020, 124, 3028.

[23] F. D. Hardcastle, I. E. Wachs, The Journal of Physical Chemistry 1991, 95, 5031.

[24] J. H. Kim, J. Lee, J. H. Kim, C. Hwang, C. Lee, J. Y. Park, Applied Physics Letters 2015, 106, 251606.

The table of contents entry should be 50−60 words long and should be written in the present tense and impersonal style (i.e., avoid we). The text should be different from the abstract text.

The hydrated Zn^{2+} intercalation into the $Mg_{0.26}V_2O_5{\cdot}0.73H_2O$ (MVO) nanobelts is reported and confirmed by in-situ Raman and FT-IR. Experiment and calculation reveal that insertion of the hydrated form of Zn^{2+}, instead of the naked cations, would lower the Coulombic repulsion at the electrode-electrolyte interface and avoids (decreases) the desolvation penalty of hydrated Zn^{2+} during the (de)intercalation process. In this way, the MVO nanobelts realize a high areal capacity of 2.12 mAh cm^{-2} at 0.05 A g^{-1}, outstanding cycling stability of 2500 cycles at 10 A g^{-1} at a high mass loading of 5 mg cm^{-2}.

Keyword: Zinc-ion battery, $Mg_{0.26}V_2O_5{\cdot}0.73H_2O$, *in-situ* FT-IR spectrum, *in-situ* Raman spectrum, zinc intercalation/deintercalation

Na Wang[1], Congli Sun[2], Xiaobing Liao[2], Yifei Yuan[3], Hongwei Cheng[1,], Qiangchao Sun[1], Bingliang Wang[4], Xuelei Pan[2], Kangning Zhao[1,2], Qian Xu[1], Xionggang Lu[1,*], Jun Lu[3,*]*

Reversible (De) intercalation of Hydrated Zn^{2+} in Mg^{2+}-Stabilized V_2O_5 Nanobelts With High Areal Capacity

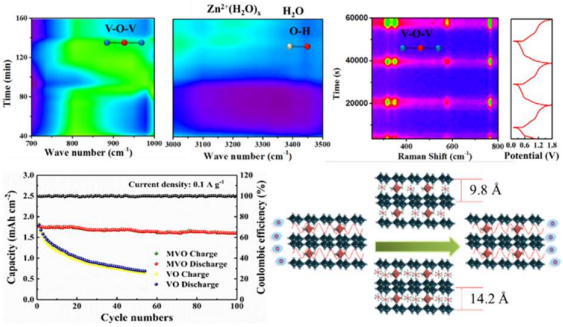

ToC figure ((Please choose one size: 55 mm broad × 50 mm high ***or*** *110 mm broad × 20 mm high. Please do not use any other dimensions))*

Supporting Information

Reversible (De) intercalation of Hydrated Zn^{2+} in Mg^{2+}-Stabilized V_2O_5 Nanobelts With High Areal Capacity

Na Wang[1], Congli Sun[2], Xiaobing Liao[2], Yifei Yuan[3], Hongwei Cheng[1,], Qiangchao Sun[1], Bingliang Wang[4], Xuelei Pan[2], Kangning Zhao[1,2], Qian Xu[1], Xionggang Lu[1,*], Jun Lu[3,*]*

N. Wang, H. Cheng, Q. Sun, K. Zhao, Q. Xu, X. Lu

State Key Laboratory of Advanced Special Steel & Shanghai Key Laboratory of Advanced Ferrometallurgy & School of Materials Science and Engineering, Shanghai University, Shanghai 200444, P. R. China

E-mail: hwcheng@shu.edu.cn (H.W. Cheng); luxg@shu.edu.cn (X.G. Lu).

C. Sun, X. Liao, X. Pan, K. Zhao

State Key Laboratory of Advanced Technology for Materials Synthesis and Processing, International School of Materials Science and Engineering, Wuhan University of Technology, Wuhan 430070, China

Y. Yuan, J. Lu

Chemical Sciences and Engineering Division, Argonne National Laboratory, Lemont, Illinois 60439, United States

E-mail: junlu@anl.gov (J. Lu)

B. Wang

Department of Chemistry, Institute of New Energy, iChEM (Collaborative Innovation Center of Chemistry for Energy Materials), Fudan University, Shanghai 200433, P. R. China

Experimental Details

1.1 Materials Synthesis

The MVO is prepared followed by the previous study. In a typical synthesis, 0.546 g V_2O_5 (AR, 99.9%) was dissolved in 24 mL distilled water with stirring at room temperature for 60 min. Then, 6.0 mL H_2O_2 (AR, 30.0%) was added and reacted violently. After stirring for about 40 min, the dark brown solution was obtained. Next, 0.214 g $C_4H_6O_4Mg{\cdot}4H_2O$ (AR, ≥ 99.0%) was dissolved in 10 mL distilled water, added to the dark brown solution above, and got homogeneous orange clear liquid after continuous stirring. Then, the orange solution was transferred into a 50 mL Teflon-lined autoclave, which was put in a constant temperature oven and maintained at 220 °C for 48 h. Afterward, when the autoclave was cooled, the precipitate washed with distilled water and alcohol several times was dried in an oven at 80 °C for 12 h in the air to acquire the $Mg_{0.26}V_2O_5{\cdot}0.73H_2O$ (MVO) nanobelts. As a comparative experiment, V_2O_5 (VO) nanowires were prepared via the same process without $C_4H_6O_4Mg{\cdot}4H_2O$.

1.2 Material Characterizations

Crystallographic structure of the samples was determined by D8 advance X-ray diffraction (XRD) measurement with Cu Kα radiation (λ = 1.54 Å) in a 2θ range from 5° to 45°. The images to characterized morphology of the products were carried out with a JSM-7500F scanning electron microscopy (SEM) and a JEM-2100F high-resolution spherical transmission electron microscopy (STEM/EDS). The X-ray photoelectron spectroscopy (XPS) was performed on an ESCALAB 250Xi to study the chemical states of the products. Fourier Transform Infrared (FT-IR) spectroscopy was conducted on a Thermo Scientific Nicolet

6700 FT-IR spectrometer and Raman spectroscopy was obtained using a RM-1000 laser Raman microscopy system.

Electrochemical Measurements

The working electrode was prepared by mixing the active material, acetylene black and polytetrafluoroethylene (PTFE) binder at a weight ratio of 7:2:1 into the isopropyl alcohol solvent. Then, the slurry was evenly ground, tableted, dried at 80 °C for 12 h, and cut into electrodes, which have a mass loading of about 5 mg cm^{-2}. The 3mol L^{-1} $Zn(CF_3SO_3)_2$ aqueous solution was used as the electrolyte. Besides, the glass fiber (GF/A) of Whatman was selected as a separator, and zinc foil was acted as the counter anode. The electrodes were fabricated with CR-2016 coin cells in the air to obtain the electrochemical performance. The charge/discharge tests were carried out on LAND CT2001A, a battery testing system. The cyclic voltammograms (CV) were tested on the Princeton Versa STAT. *In-situ* Raman was carried out on a Horiba LabRAM HR Evolution Raman. *In situ* ATR FT-IR characterization was conducted using a FT-IR spectrometer (Nicolet 6700, Thermo-Fisher Scientific) with an extended range diamond ATR accessory (Shanghai Linglu Instrument Co., Ltd.). All FT-IR spectrum was collected using a deuterated triglycine sulfate (DTGS) detector at a resolution of 256 scans per spectrum at 4 cm^{-1}.

Calculation Details. All density functional theory (DFT)[1, 2] calculations were operated at the Vienna ab-initio simulation package (VASP5.4)[3], using the projector augmented wave (PAW) method, and the generalized gradient approximation (GGA) with the Perdew-Burke-Ernzerhof (PBE)[4] functional was applied for the exchange-correlation functional.

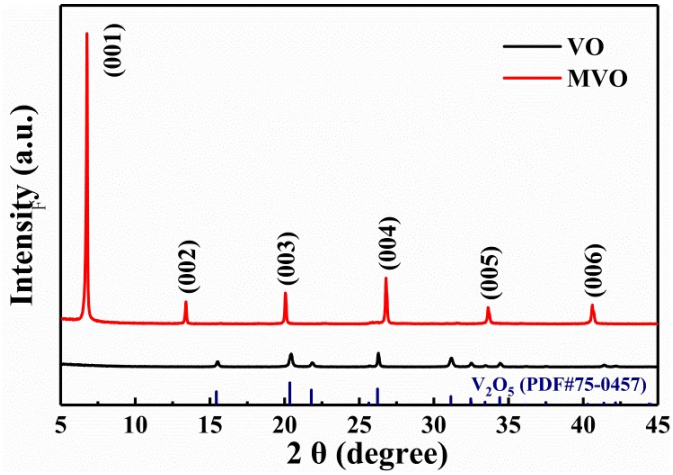

Fig. S1. XRD pattern of the VO and the MVO.

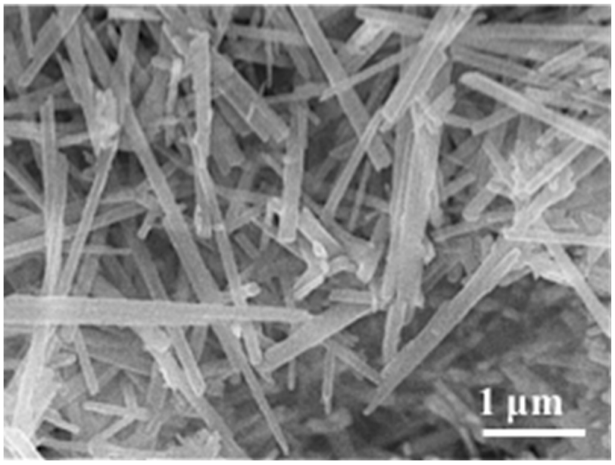

Fig. S2. SEM image of the MVO electrode.

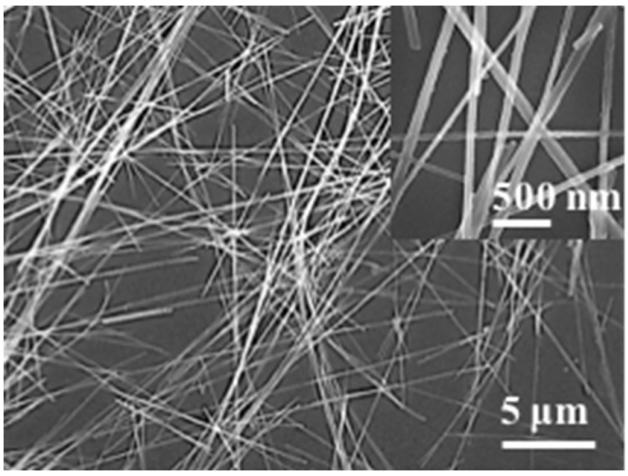

Fig. S3. SEM image of the VO electrode.

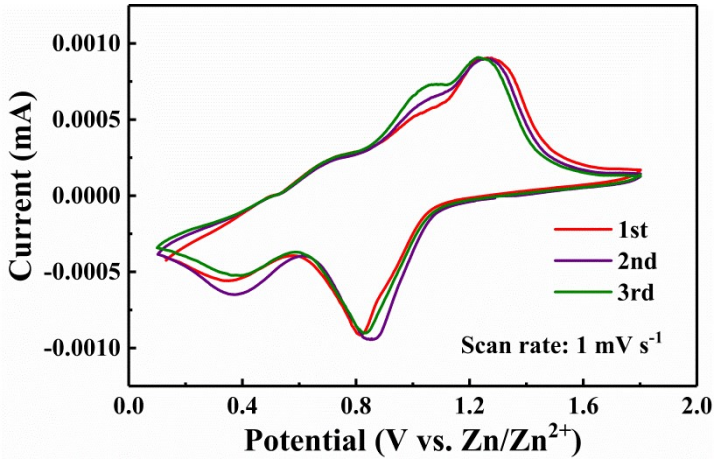

Fig. S4. CV curves of the VO electrode.

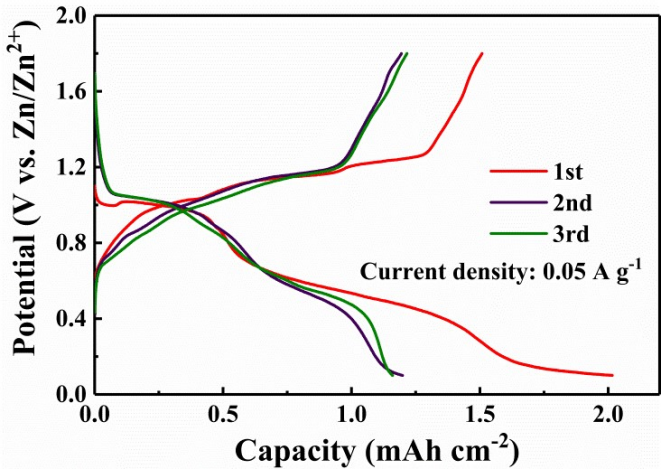

Fig. S5. Charge/discharge curves of the VO at 0.05 A g^{-1}.

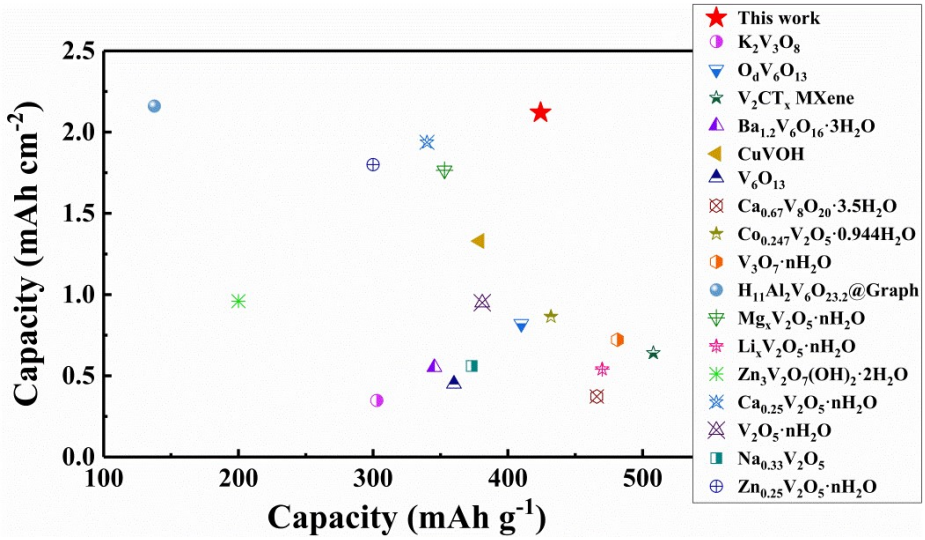

Fig. S6. The comparison of MVO and other vanadium-based electrodes.

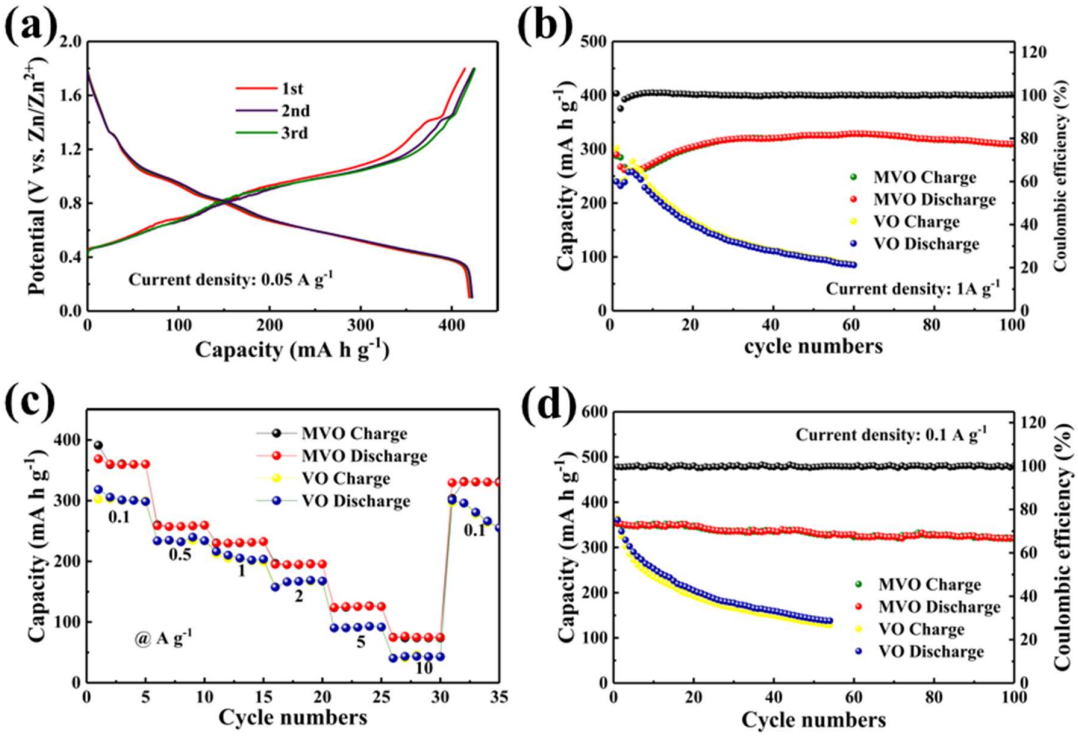

Fig. S7. The weight capacity of MVO.

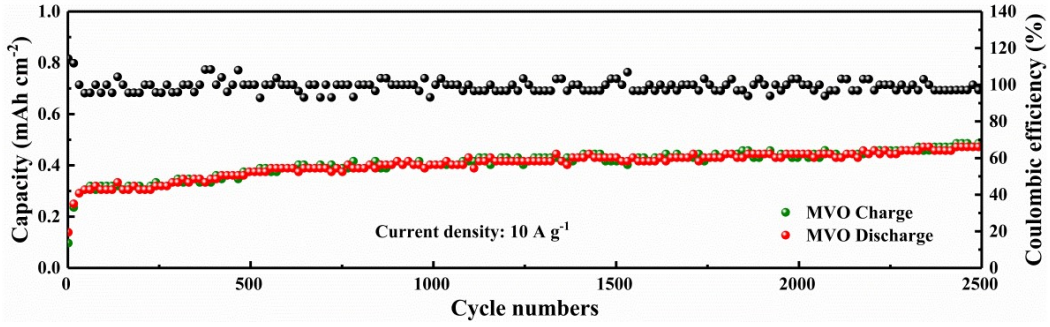

Fig. S8. Cycling performance of MVO at 10 A g^{-1}.

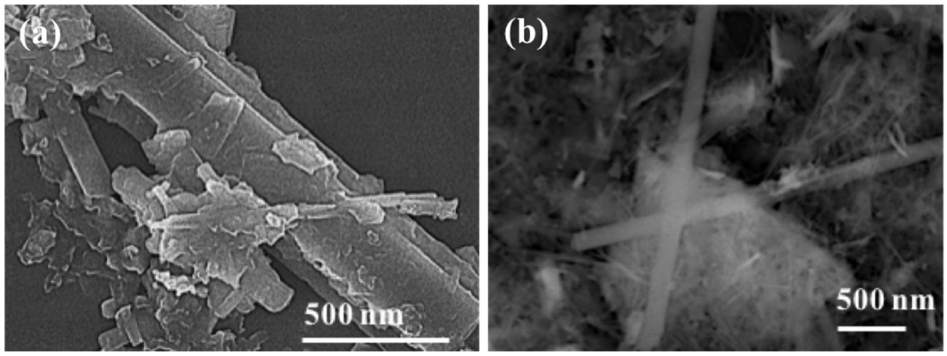

Fig. S9. (a) SEM image of MVO after 200 cycles at 0.1 A g^{-1}, SEM image of MVO after 2500 cycles at 10 A g^{-1}.

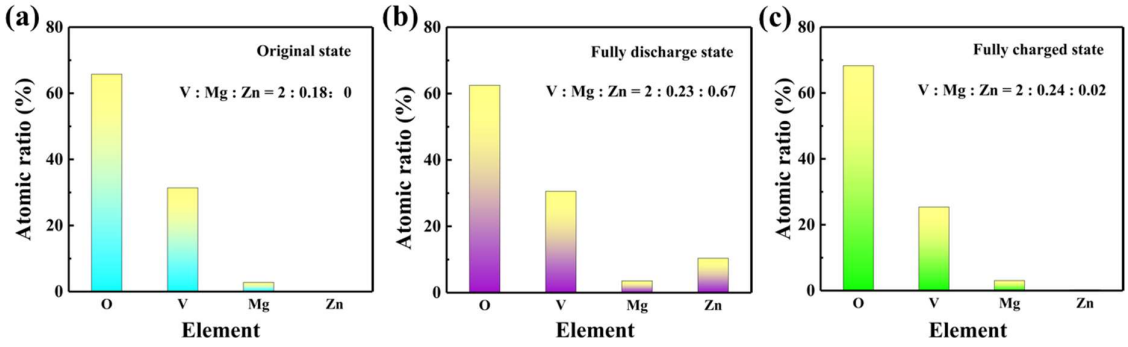

Fig. S10. (a)-(c) The EDS quantification of every element in different states.

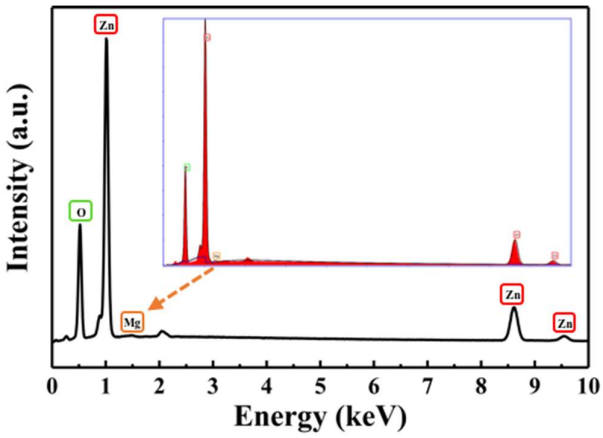

Fig. S11. Energy dispersive X-ray (EDX) spectrum of the Zn anode after 200 cycles at 1 A g^{-1}.

ab. S1. Electrochemical performances of recently reported vanadium-based zinc-ion battery cathode materials.

Cathode	Capacity (mA h cm^{-2}) at x A g^{-1}	Mass loading (mg cm^{-2})	Capacity retention after n cycles at y A g^{-1}	Ref.
$Mg_{0.26}V_2O_5 \cdot 0.73H_2O$	2.12 (x=0.05)	5	98% (n=2000, y=5)	This work
$K_2V_3O_8$	0.35 (x=0.1)	1.15	92.3% (n=2000, y=4)	5
$O_dV_6O_{13}$	0.82 (x=0.2)	2	86% (n=2000, y=2)	6
V_2CT_x Mxene	0.64 (x=0.2)	1-1.5	/	7
$Ba_{1.2}V_6O_{16} \cdot 3H_2O$	~0.55 (x=0.1)	1.2-2	95.6% (n=2000, y=5)	8
CuVOH	1.33 (x=0.5)	3-4	93% (n=1000, y=4)	9
V_6O_{13}	~0.45 (x=0.2)	1-1.5	92% (n=2000, y=4)	10
$Ca_{0.67}V_8O_{20} \cdot 3.5H_2O$	0.37 (x=0.1)	0.8	74% (n=2000, y=5)	11
$Co_{0.247}V_2O_5 \cdot 0.944H_2O$	0.86 (x=0.1)	1-3	90.26% (n=7500, y=4)	12
$V_3O_7 \cdot H_2O$	0.72 (x=0.1)	1-2	85.4% (n=1000, y=5)	13
$H_{11}Al_2V_6O_{23.2}$@Graphene	2.1 (x=2)	15.7	95.7% (n=400, y=2)	14
$Mg_xV_2O_5 \cdot nH_2O$	~1.77 (x=0.05)	5-7	97% (n=2000, y=5)	15
$Li_xV_2O_5 \cdot nH_2O$	~0.53 (x=0.1)	0.9-1.2	92% (n=500, y=5)	16
$Zn_3V_2O_7(OH)_2 \cdot 2H_2O$	~0.96 (x=0.05)	4-5	68% (n=300, y=0.2)	17
$Ca_{0.25}V_2O_5 \cdot nH_2O$	1.94 (x=0.05)	5.7	96% (n=3000, y=20)	18
$V_2O_5 \cdot nH_2O$	0.95 (x=0.06)	2.5	71% (n=900, y=6)	19
$Na_{0.33}V_2O_5$	0.56 (x=0.2)	1-2	93% (n=1000, y=1)	20
$Zn_{0.25}V_2O_5 \cdot nH_2O$	1.8 (x=0.05)	5-7	80% (n=1000, y=2.4)	21

Tab. S2. XRD refinement for $Mg_{0.26}V_2O_5 \cdot 0.73H_2O$

Diffractometer	Bruker D8 Advance
Radiation	Cu Kα
2θ range	5 ~ 45°
Step size	0.02
Space group	P1
A	10.59 Å
B	8.03 Å
C	13.39 Å
A	91.39°
B	90.77
Γ	88.86
Cell volume	1137 $Å^3$
Rwp	6.23 %

Atomic positions and occupancies were not refined due to the high degree of preferred orientation present in the diffraction data.

Tab. S3. The ICP-OES analysis of MVO

Elements	Content (mg L^{-1})
Mg	2.69
V	43.14

Tab. S4. Calculation details of hydrated level zinc through GGA+PBE and M06

GGA+PBE			
	energy (Ha)	ΔE(eV)	Etotal (eV)
Zn	-1779.23443		
H_2O	-76.3880741		
$Zn(H_2O)_2$	-1931.62482		
$Zn(H_2O)_3$	-2008.07042	1.565255929	-8.931812042
$Zn(H_2O)_4$	-2084.50135	1.166362282	-7.76544976
$Zn(H_2O)_5$	-2160.91001	0.559982961	-7.205466799
$Zn(H_2O)_6$	-2237.31742	0.526166341	-6.679300457

M06			
	energy (Ha)	ΔE(eV)	Etotal (eV)
Zn	-1779.23443		
H_2O	-76.454916		
$Zn(H_2O)_2$	-1931.95397		
$Zn(H_2O)_3$	-2008.46484	1.522596582	-3.655537515
$Zn(H_2O)_4$	-2084.96316	1.181045183	-2.474492333
$Zn(H_2O)_5$	-2161.44263	0.668036239	-1.806456094
$Zn(H_2O)_6$	-2237.92162	0.6551563	-1.151299794

Reference

[1] G. Kresse, J. Furthmiiller. Efficiency of ab-initio total energy calculations for metals and semiconductors using a plane-wave basis set. Comput. Mater. Sci. 1996, 6, 15-50

[2] S. Grimme. Semiempirical GGA-type density functional constructed with a long-range dispersion correction. J. Compu. Chem. 2006, 27, 1787-1799

[3] G. Kresse. Efficient iterative schemes for ab initio total-energy calculations using a plane-wave basis set. Phys. Rev. B. 1996, 54, 16

[4] P. E. Blöchl. Projector augmented-wave method. Phys. Rev. B. 1994, 50, 17953-17979

[5] Z. Li, B. Wu, M. Yan, et al. Novel Charging-Optimized Cathode for a Fast and High-Capacity Zinc-Ion Battery. ACS Appl. Mater. Int. 2020, 12, 10420-10427

[6] M. Liao, J. Wang, L. Ye, et al. A Deep-Cycle Aqueous Zinc-Ion Battery Containing an Oxygen-Deficient Vanadium Oxide Cathode. Angew. Chem. Int. Ed. 2020, 59, 2273-2278

[7] X. Li, M. Li, Q. Yang, et al. Phase Transition Induced Unusual Electrochemical Performance of V_2CTX MXene for Aqueous Zinc Hybrid-Ion Battery. ACS Nano. 2020, DOI: 10.1021/acsnano.9b06866

[8] X. Wang, B. Xi, X. Ma, et al. Boosting Zinc-Ion Storage Capability by Effectively Suppressing Vanadium Dissolution Based on Robust Layered Barium Vanadate. Nano Lett. 2020, https://dx.doi.org/10.1021/acs.nanolett.0c00732

[9] C. Liu, M. Tian, M. Wang, et al. Catalyzing zinc-ion intercalation in hydrated vanadates for aqueous zinc-ion batteries. J. Mater. Chem. A. 2020, DOI: 10.1039/D0TA01468K

[10] J. Shin, D. S. Choi, H. J. Lee, et al. Hydrated intercalation for high-performance aqueous zinc ion batteries. Adv. Energy Mater. 2019, 1900083

[11] K. Zhu, T. Wu, K. Huang. A high capacity bilayer cathode for aqueous Zn-ion batteries. ACS Nano. 2019, DOI: 10.1021/acsnano.9b08039

[12] L. Ma, N. Li, C. Long, et al. Achieving both high voltage and high capacity in aqueous zinc-ion battery for record high energy density. Adv. Funct. Mater. 2019, 1906142

[13] Z. Cao, H. Chu, H. Zhang, et al. An in situ electrochemical oxidation strategy for formation of nanogrid-shaped $V_3O_7{\cdot}H_2O$ with enhanced zinc storage properties. J. Mater. Chem. A. 2019, 7, 25262

[14] W. Zhang, S. Liang, G. Fang, et al. Ultra-high mass-loading cathode for aqueous zinc-ion battery based on graphene-wrapped aluminum vanadate nanobelts. Nano-Micro Lett. 2019, 11, 69

[15] F. Ming, H. Liang, Y. Lei, et al. Layered $Mg_xV_2O_5{\cdot}nH_2O$ as Cathode Material for High-Performance Aqueous Zinc Ion Batteries. ACS Energy Lett. 2018, 3, 2602-2609

[16] Y. Yang, Y. Tang, G. Fang, et al. Li^+ intercalated $V_2O_5{\cdot}nH_2O$ with enlarged layer spacing and fast ion diffusion as an aqueous zinc-ion battery cathode. Energy Environ. Sci. 2018, 11, 3157

[17] C. Xia, J. Guo, Y. Lei, et al. Rechargeable aqueous zinc-ion battery based on porous framework zinc pyrovanadate intercalation cathode. Adv. Mater. 2018, 30, 1705580

[18] C Xia, J. Guo, P. Li, et al. Highly stable aqueous zinc-ion storage using layered calcium vanadium oxide bronze cathode. Angew. Chem. Int. Ed. 2018, 130, 4007-4012

[19] M. Yan, P. He, Y. Chen, et al. Water-Lubricated intercalation in $V_2O_5{\cdot}nH_2O$ for high-capacity and high-rate aqueous rechargeable zinc batteries. Adv. Mater. 2018, 30, 1703725

[20] P. He, G. Zhang, X. Liao, et al. Sodium ion stabilized vanadium oxide nanowire cathode for high-performance zinc-ion batteries. Adv. Energy Mater. 2018, 8, 1702463

[21] D. Kundu, B. D. Adams, V. Duffort, et al. A high-capacity and long-life aqueous rechargeable zinc battery using a metal oxide intercalation cathode. Nature Energy. 2016, 1, 16119